Towards Passive Aeroelastic Tailoring of Large Wind Turbines Using High-Fidelity Multidisciplinary Design Optimization

Marco Mangano*[1], Sicheng He†[1], Yingqian Liao‡[1], Denis-Gabriel Caprace§[2], and Joaquim R. R. A. Martins¶[1]
[1]*University of Michigan, Ann Arbor, Michigan, United States*
[2]*Brigham Young University, Provo, Utah, United States*

The decarbonization of the electric grid is a fundamental technological and socio-economical challenge to address the looming threat of climate change. The reduction of the levelized cost of energy is a critical step to expand the application of carbon-free technologies that rely on high-potential, renewable energy sources such as wind power. Advanced computational tools are instrumental to capturing the tightly-coupled, multi-physics interactions that characterize modern highly-flexible wind turbine rotors. In this work, we use our high-fidelity multidisciplinary design optimization software to perform aerostructural optimization studies of a large wind turbine configuration, using an efficient, highly-scalable, gradient-based approach on a coupled CFD/FEM model. We investigate the trade-offs between steady-state aerodynamic efficiency and structural cost of a benchmark rotor using more than 100 structural and geometric design variables. Mass and torque are simultaneously used as performance metrics as we constrain the maximum stress and tip displacement of the rotor at below-rated operating conditions. We discuss both the optimized design features and the general design trends in the form of Pareto front analyses as we sweep over different prescribed torque values and objective weights. The results highlight the benefits of the coupled model with respect to a single-discipline strategy and showcase the additional insight that high-fidelity analysis tools offer to designers. As we work towards a more refined structural model and the inclusion of a larger set of shape variables to extend the optimization capabilities of the tool, the results support the idea that such high-fidelity approaches can complement conventional low-fidelity tools in the design of light and efficient turbine blades.

I. Nomenclature

AEP	=	annual energy production
A_r	=	swept area
C_P	=	power coefficient
d_{tip}	=	blade tip flapwise displacement
$\mathbf{f}(\mathbf{x})$	=	generic objective function
$\mathbf{g}(\mathbf{x})$	=	generic constraint
$\text{KS}_{\sigma_{\max}}$	=	aggregated stress constraint
$\text{KS}_{d_{\text{tip}}}$	=	aggregated tip displacement constraint
LCOE	=	levelized cost of energy
M_1	=	aerodynamic performance metric
M_2	=	mass-based cost metric
M_{eq}	=	equivalent mass of steel
m	=	mass of the rotor
Q_x	=	torque extracted from the rotor

*Ph.D candidate, Department of Aerospace Engineering, AIAA Student Member.
†Post-doctoral Research Fellow, Department of Aerospace Engineering, AIAA Member.
‡Post-doctoral Research Fellow, Department of Aerospace Engineering.
§Post-doctoral Researcher, Department of Mechanical engineering. AIAA Member.
¶Professor, Department of Aerospace Engineering, AIAA Fellow.

TSR	=	tip speed ratio
V	=	inflow velocity
$\mathbf{x}$	=	vector of design variables
$\mathbf{x_{st}}$	=	structural panel thickness
$\boldsymbol{\theta}$	=	twist angle

II. Introduction

The climate science community overwhelmingly agrees that human activities, intensive greenhouse gasses emissions in the first place, are dramatically affecting the thermochemical equilibrium of our atmosphere. A recent report from the Intergovernmental Panel on Climate Change (IPCC) [1] suggests that we have already left the global temperature range of the Holocene, with yet inestimable negative consequences affecting natural resources availability, industrial-scale food production, and ultimately the individual well-being of the current and future generations. Net-zero emission targets have been recently outlined by the International Energy Agency [2] to curb global warming and reverse the effects of the last two centuries of industrial emissions, exacerbated by intensive fossil fuels consumption and loosely-regulated growth. To achieve this goal and limit the global temperature increase to 1.5° by the end of the century, it is of uttermost importance to accelerate the transition to affordable carbon-free energy sources and minimize the impact of human activities on a global scale in the next few decades. The pathway proposed by IEA, in particular, suggests that almost 70% of the energy production in 2050 will come from solar and wind resources.

Wind energy is currently regarded as a mature technology at an industrial scale in both its onshore and offshore configurations. However, similar to other carbon-free energy sources, resource intermittency and installation-site dependency are limiting the current amount of energy that can be extracted. Recent studies from NREL [3] and IRENA [4] highlight how there is a large and currently untouched potential for locating wind energy further away from the coastline, where the wind resource is more abundant and steady, but the sea depth prevents the deployment of the fixed-bottom wind farm. Large floating offshore wind turbines (FOWT) are a promising solution to capture this resource and further reduce the cost of carbon-free energy.

The design of current and planned floating projects relies on experience gathered from previous bottom-fixed turbine configurations. However, the different environmental conditions, together with unique deployment and operations characteristics, strongly suggest that wind turbine configurations must be designed to maximize the market advantage of FOWT. On the one hand, the interactions of aerodynamics, hydrodynamics, structural and control systems need to be carefully modeled with tightly-coupled multidisciplinary analyses. On the other hand, the installation location relaxes the stringent noise and transportation constraints affecting the land-based counterparts, enabling the development of large-diameter, low-solidity rotors that maximize the aerodynamic performance and, consequently, the power extraction [5].

To accelerate the development of these new configurations, computational tools are essential to capture the multi-physics interactions that drive the performance and the structural sizing of these complex systems. The traditional "sequential" design of aerodynamic shape and internal structure falls short of taking full advantage of the interaction between fluid and structural dynamics [6–8]. Control co-design and multidisciplinary design optimization (MDO) techniques can exploit multi-physics trade-offs to minimize the mass of a highly-efficient floating system, with major benefits for capital investments, deployment, and operational benefits [9].

The research we present is part of the ARPA-E ATLANTIS project, whose goal is to "design radically new FOWT by maximizing their rotor-area-to-total-weight ratio while maintaining or ideally increasing turbine generation efficiency" *. Within a broader research team considering a holistic design approach to turbine design, our goal is to leverage high-fidelity MDO to enable the preliminary design of the large rotors with unprecedented design insight. The University of Michigan's MDO Lab has developed a high-fidelity multidisciplinary optimization tool named MACH [10] that uses a set of parametrization and analysis modules to perform gradient-based optimization. A previous collaboration with the Technical University of Denmark (DTU) has extended our tool capabilities to rotating lifting components and explored the potential of aerodynamic shape optimization of a wind turbine using a Computational Fluid Dynamics (CFD) code [11]. The authors investigated the advantages of a RANS-based approach to enhance the performance of a

*ATLANTIS Project web page

turbine rotor using a large set of design variables to tailor both its planform and cross-sectional shape. This paper builds on top of that work, extending the analysis and optimization to a tightly-coupled, steady-state aerostructural model.

The combination of CFD and Finite Element Method (FEM) tools extends the set of design variables that can be used in optimization and circumvents some of the assumptions that limit the modeling capabilities of conventional Blade Element Momentum Theory (BEMT) and beam theory-based design tools. This approach, combined with such tools and advanced control strategies, has the potential to maximize the performance and minimize the design costs of the next generation of wind turbines considering both steady-state and life-cycle performance and operations. While wind turbine optimization is not a new concept, we propose a first-of-a-kind application of high-fidelity aerostructural optimization tools in the design cycle of a large turbine rotor.

The authors are aware how high-fidelity optimization can quickly become intractable when a high number of design points are simultaneously evaluated —regardless of how efficiently the analysis code is implemented within the optimization framework. To address this shortcoming, the present work can be extended with a mixed-fidelity strategy to combine high-fidelity and conventional BEMT-based approaches in the optimization process [12]. In the latter reference, OpenFAST is coupled to MACH to extend its analysis capabilities to unsteady flow conditions and include life-cycle considerations in the design of the blade, enabling high-fidelity optimization compliant with fatigue and extreme load conditions.

A. A Short Overview of the State-of-the-art for Wind Turbine Design Optimization

In recent years, several tools have been developed to support the (conceptual) design of current and future wind turbines configurations. The state-of-the-art software, such as OpenFAST [13], Cp-Max [6], HAWTopt2 [14], and more recently ATOM [15], SHARPy [16], Qblade [17], and MoWit [18], are capable of simulating the full turbine, from flexible rotor and tower to the platform and mooring systems for floating concepts. Linear and nonlinear controllers are also included in the analysis, for both development purposes and more realistic operating performance evaluation. Such a holistic approach is necessary to capture the multi-body dynamics of the system and the unsteady aerostructural phenomena driving the performance and sizing of a turbine over its planned operating life. We will refer to these tools as "conventional" to make a distinction with the CFD and FEM software used in this work.

These conventional tools often rely on a combination of low-fidelity solvers to model the different components of the wind turbine. The aforementioned OpenFAST (and its predecessor FAST) have set the standard for turbine analyses in the last few years, combining a modal and multibody-dynamics formulation to include all the system macro components. On the structural side, the beam models used by BeamDyn and ElastoDyn can capture the dynamic response of the turbine but are limited in terms of degrees of freedom (ElastoDyn) and local stresses estimation (both). The aerodynamic analysis tool AeroDyn, based on the blade element momentum theory (BEMT), has shown good experimental agreement with conventional designs. However, the model assumptions prevent the application of this method to larger blades where 3D effects are prominent, especially at the root and tip. Moreover, the use of predetermined wing section polars "freezes" the airfoil design over successive iterations, and the absence of accurate sensitivity information has limited its application in optimization contexts.

Several works combined high and low-fidelity tools to find a trade-off between accuracy and computational cost. Finite-element structural models have been coupled with a hybrid lifting-line/vortex method in a multi-body aero-hydro-servo-elastic model by [19], showing good agreement with [20] and paving the way for relatively cheap strategies to overcome BEMT limitations. To address the same trade-off and overcome the limitations of BEMT models, in the last few years, "mid-fidelity" aerodynamic approaches such as vortex-particle methods have been introduced [21], although few relevant publications are currently available.

Other recent works shifted the focus to a narrower but higher-fidelity approach, highlighting the necessity of capturing the complex fluid-structure interaction on modern blades [22]. Recently Wainwright et al. [23] leveraged GPU acceleration techniques to study the aerostructural behavior of a rotor in complex inflow conditions combining a commercial CFD software and a finite-element modal solver. The authors used a strong coupling strategy to resolve time-accurate analyses, using a radial basis function approach to pass load-transfer information between the solvers. A work by Cheng et al. [24] validated a model that couples an actuator line model, an aerodynamic RANS solver, and an hydrodynamic CFD tool in OpenFOAM to study the behavior of a floating wind turbine. While BEMT and beam models have limitations on accurately predicting performance in complex flow, high-fidelity codes are limited by their computational cost and hardness of implementation. Despite the promising results of high-fidelity simulations, at the

current stage, none of these high-fidelity models has been used within an optimization framework.

While the works presented above aimed at a holistic analysis approach, other research groups have focused specifically on design optimization problems. Gray et al. [25] and Ning and Petch [26] have shown how analytical gradients can be effectively used for optimization problems that go beyond the sole rotor design and include a larger set of constraints. The problem formulation (and architecture more in general) has been extended to include fatigue considerations in the structural sizing [27]. Bottasso et al. [28] proposed a bi-level design approach in the form of a loosely-coupled nested optimization, using a holistic turbine model with a broad range of design constraints. The solution that maximizes the AEP/weight objective is found by interpolating a family of designs generated via low-fidelity, finite-differences gradient-based optimization. A more compact sequential approach using the same tool is presented in [29], while another work from the same research group [6] extended the model towards a monolithic approach that includes a more accurate FEM analysis to evaluate the structural properties of selected blade cross-sections. This method was effective, but the model coupling assumptions hindered the optimization robustness. To circumvent the implementation challenges of a tightly coupled aerostructural approach, these works use a fixed set of "optimized" aerodynamic loads in between structural optimization sub-iterations, ultimately converging to a consistent design. A similar approach has been used recently by Scott et al. [30] for the sequential optimization of a large turbine using a linearized aerostructural model to speed up aero-servo-elastic simulations. Zahle et al. [14] and McWilliam et al. [31] showed the potential of aeroelastic tailoring and passive load alleviation in blade design, leveraging on composite material anisotropic behavior. Although they used conventional low-fidelity models and finite-difference gradients, which ultimately limit the accuracy and robustness of the optimization, their results were promising. The coupling of a CFD and an aeroelastic solver has been investigated by Heinz et al. [20], showing good agreement with conventional approaches despite a non-conservative force transfer scheme and a loosely-coupled aerostructural solution. Commercial CFD codes and reduced-order structural models have also been used to explore the blade-tower interactions to quantify acceptable tip clearances and efficiency losses [32].

B. Paper Outline

In summary, this work presents a first-of-a-kind aerostructural optimization study for a large wind turbine rotor using a coupled CFD/FEM solver. We leverage the higher fidelity of our aerodynamic and structural analysis software and its efficient implementation in a gradient-based optimization framework to capture steady-state aeroelastic interactions over the rotor of the DTU 10MW configuration. Several optimization problems are investigated, culminating in an MDO problem where we use hundreds of aerodynamic and structural design variables to concurrently maximize the aerodynamic efficiency of the rotor while minimizing its mass. Ultimately, we show how the high-fidelity tight aerostructural coupling enables the identification of better designs that conventional optimization approaches might not identify due to their underlying modeling and coupling assumptions.

In the following sections, we present our tool in more detail in Sec. III and discuss our problem formulation in Sec. V where we define the objective, constraints, and design variables of our study. The results in Sec. VI are broken down into: a set of uncoupled structural optimization cases for preliminary sizing of our model in Sec. VI.B, a brief discussion of a coupled analysis in Sec. VI.A, a set of torque- and displacement-constrained mass minimization problems in Sec. VI.C, and a set of MDO cases with different weighted objective function in Sec. VI.D. The key takeaways of our approach are finally summarized in Sec. VII.

III. Methodology

Despite the increase in the computational cost and implementation effort, high-fidelity solvers offer higher result accuracy and more refined model definition than their low-fidelity counterparts, such as blade element momentum theory and beam models, which are generally bounded by stronger physical assumptions. Engineers can use these high-fidelity tools to gain better design insight and extend the available design space with a higher number of design variables. Gradient-based optimization techniques are the only viable strategy to turn high-dimensional and high-fidelity optimization formulations into a tractable numerical problem [8, 33]. The use of adjoint-based derivatives calculations for the coupled system decouples the overall computational cost from the number of design variables, making such solvers suitable for optimizations with $N_{\text{Design Variables}} \gg N_{\text{Functions of interest}}$.

We propose to use our MDO framework, MACH, to perform extensive aerostructural optimization studies using

high-fidelity CFD and FEM analysis tools. This framework has been extensively used in previous works from the MDO Lab. Most of these previous works focused on aircraft design problems [34, 35], while a few others are extended to hydrofoil design [36]. In this paper, we apply the same methodology to a high-fidelity wind turbine aerostructural model to demonstrate the potential performance and mass reduction benefits of integrating this approach in rotor blade design.

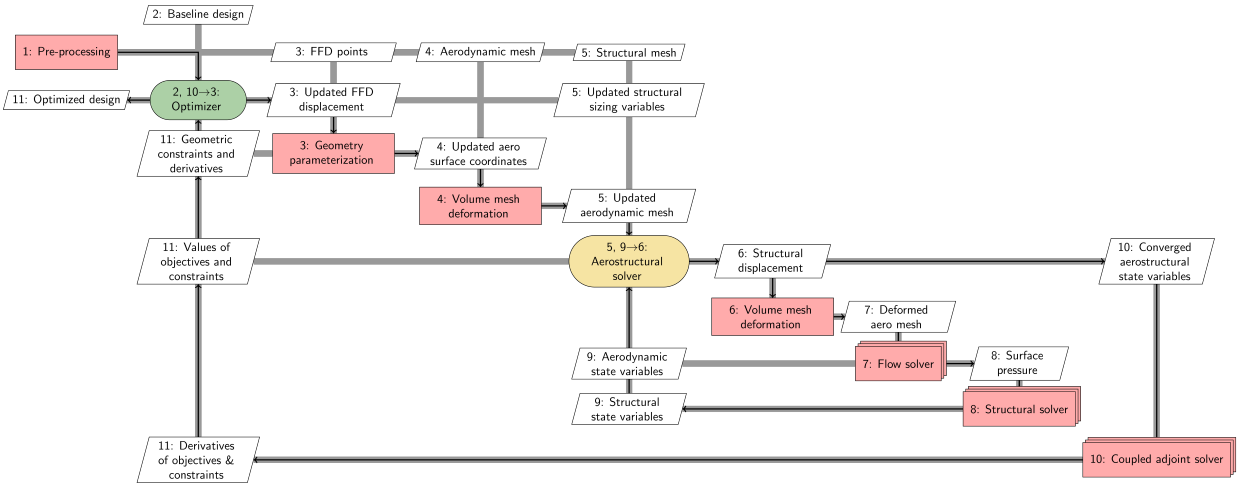

Fig. 1 XDSM diagram of MACH optimization framework.

As shown in the Extended Design Structure Matrix (XDSM) diagram [37] in Fig. 1, MACH is composed of several tightly-integrated sub-modules that enable geometry parametrization and deformation, coupled aerostructural analysis, and efficient derivatives evaluation in an optimization context. The open-source, version of our toolkit, MACH-Aero [†] has been applied to a broader range of aerodynamic shape optimization studies including unconventional aircraft configurations [38–40], hydrofoil optimization [41], and wind turbine configurations [11, 42]. In the following paragraphs, we briefly introduce the main components of the framework. The benchmark is further discussed in Sec. IV.

A. Geometry Parametrization - pyGeo

The geometry manipulation module, pyGeo [‡], is based on the Free-Form Deformation (FFD) approach. This approach was first described by Sederberg and Parry [43] and later implemented by Kenway et al. [44] in pyGeo. A control volume is defined by the user starting from a 3D distribution of control points, which are effectively used as design variables by the optimizer. The input meshes for the solvers of interest are defined in a pre-processing stage and embedded in this control volume. The displacements of the control points are propagated to the embedded geometry as if it was immersed in a "flexible, transparent jelly" [43]. From a mathematical perspective, the point interpolation is obtained with a Non-Uniform Rational B-Splines (NURBS) scheme. This approach is advantageous as it is baseline-configuration-agnostic and facilitates the implementation of adjoint-based derivatives.

B. Mesh Deformation - IDwarp

The process of regenerating CFD or FEM mesh at every geometry update is costly and poses a higher risk of mesh failures for complex geometries when using an automated process. To avoid this, a dedicated module called IDwarp [§] ensures the correct propagation of the surface nodes displacements from the updated geometry to the volume mesh using an inexact explicit interpolation algorithm based on inverse distance weighting method [45]. This mesh update comes with a negligible impact on the overall computational cost [46].

[†] https://github.com/mdolab/MACH-Aero
[‡] https://github.com/mdolab/pygeo
[§] https://github.com/mdolab/idwarp

C. Aerodynamic Solver - ADflow

ADflow [¶] is a finite-volume, second-order CFD solver developed at the MDO Lab [47]. This solver includes an efficient formulation to calculate flow derivatives via the adjoint method [48], which makes it ideal for gradient-based optimization. Although originally designed for the transonic flow regime, the implementation of a low-speed preconditioner and an approximate Newton–Krylov method [49] enables the analysis of incompressible flow regimes [11, 50]. Although ADflow has time-accurate-[51] and time-spectral-[52] capabilities, for this work we will focus on steady-state, fully-turbulent inflow conditions. The Spalart–Allmaras [53, 54] turbulence model is selected for our studies.

D. Structural Solver - TACS

The structural solver used in this work is the Toolkit for the Analysis of Composite Structures (TACS) [55]. TACS can handle both linear and nonlinear geometric structural problems. In this work, we focus on linear problems. We will work towards nonlinear cases in the future. To solve the linear elastic equation, we can use both the Krylov subspace method and the direct method. The direct method is composed of three steps. The first step is to construct a local Schur complement matrix, where the internal degree-of-freedoms (DOF)s are factored out while the external DOFs are kept. Then, the Schur complement matrices from each processor are assembled into a global matrix. Finally, an LU decomposition is conducted over the global Schur matrix. In the last step, the global Schur matrix is stored in a cyclic pattern. TACS is also able to compute the derivative using Jacobi–Davidson method and Lanczos method [56, 57]. Recently, the solvers have been used to solve flutter problems [58, 59]. TACS enables several constraints for structural safety considerations. In this work, we consider a yield constraint to avoid material failure and a flapwise bending displacement constraint to maintain a safe distance between blades and the tower. For the yield constraint, we consider von Mises constraint for alloy and a maximum-strain constraint for composite models [60]. For the displacement constraint, we consider the maximum tip flapwise displacement.

Since there is a large number of yield and displacement constraints to be enforced, we apply the Kreisselmeier—Steinhauser (KS) aggregation method to obtain a smooth approximation of the maximum value of constraints [61, 62].

E. Aerostructural Solver - pyAeroStructure

The aerostructural problem can be solved using either nonlinear block Gauss–Seidel (NLBGS) or a combination of NLBGS and coupled Newton–Krylov (CNK) method. For the CNK method, a block Jacobi preconditioner is applied, where the aerodynamic and structural preconditioners are used. The derivative is computed using either linear block Gauss–Seidel (LBGS) or coupled Krylov (CK) subspace method. We use the NLBGS algorithm in this paper as the model does not show convergence issues for either the primal or the adjoint solve. More details on the algorithms can be found in the previous paper by Kenway et al. [10]. This framework has recently been extended to solve the aeroelastic limit cycle oscillation problem [63–65].

F. Optimization Wrapper - pyOptSparse

The optimization problem definition and the data flow between the solvers and the optimizer is handled by pyOptSparse [‖] [66], a python toolkit that includes wrappers for several open-source and commercial optimization algorithms, including both gradient-based and gradient-free options. The preferred optimizer for our aerostructural studies is SNOPT [67]. One of the ad-hoc solutions for the gradient-based high-fidelity optimization problem implemented in pyOptSparse is the capability to handle the constraint Jacobian in a sparse format, exploiting the computational speed-up offered by SNOPT.

IV. Baseline Turbine Rotor Configuration

In this study, we use the DTU 10 MW rotor configuration as the baseline design for our optimizations, building on the work by Madsen et al. [11]. It is a three-blade rotor with a diameter of 178.3 m and a tailored chord, airfoil, and twist distribution. The outer mold line and structural layup are defined by Bak et al. [68]. To limit the pre-processing effort and prevent major convergence challenges for ADflow [42], the geometry we are using consists of the three

[¶] https://github.com/mdolab/adflow

[‖] https://github.com/mdolab/pyoptsparse

blades "blended" together at the root, neglecting the effects of the hub on the aerodynamic performance. Although the aerodynamic blade-nacelle interactions are a relevant design factor, they have limited impact on the extracted torque for large turbines and do not influence the structural sizing of the blades. Tower-blade interactions are also neglected. Our simulations use the same aerodynamic meshes as employed in [11]. A family of four meshes was defined, starting from the most refined L0 (14 155 776 cells), up to L3 in increasing coarsening levels. Between L0 and L1 meshes, we remove every other node in the three dimensions, effectively reducing the number of cells by a factor 8. This is repeated for L2 and L3 grids as well. As noted in [11], this mesh family is particularly sensitive to grid resolution when used by ADflow at an incompressible flow regime. In this paper, we use the two coarsest meshes L2 and L3 to contain the computational cost, leaving more accurate and expensive simulations for future work. The L2 mesh has 221 184 volume nodes and converges in approximately 4.6 CPU hours, while the L3 mesh can be run on a local desktop in the order of a few minutes.

A. Structural Model

As for the structural mesh, we generate an ad-hoc structural finite-element mesh that follows the contour of the outer mold line and includes an internal main shear web and a reinforcement spar in the trailing edge area as described by Bak et al. [68]. Thin CQUAD hexahedral shell elements are used for the whole set of structural components. Three identical blades are fixed at the root, located at approximately 3 m from the rotation axis.

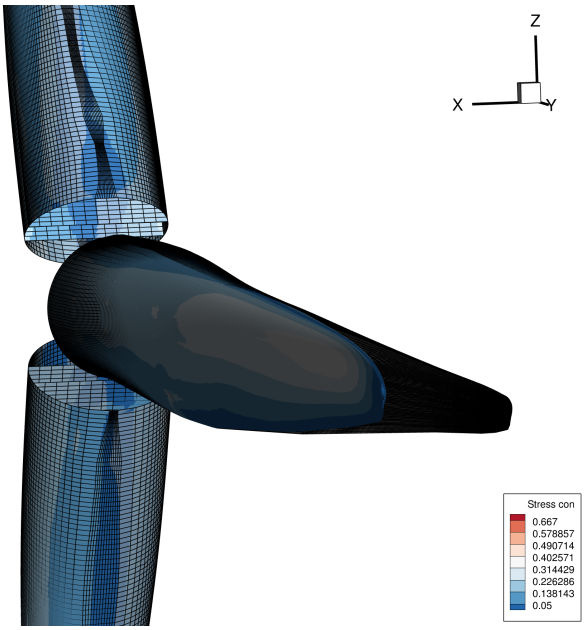

Fig. 2 Results of an analysis on the current FEM model using TACS, highlighting structural deflections and normalized stress constraint based on von Mises criterion.

The reference mesh is the same for every study presented in Sec. VI, but we developed three different structural models that differ for design variables definition and material properties. Two of these models use isotropic shell elements with aluminum density and stiffness properties. They differ in the way the design variables are defined, with one model having independent design variables for upper and lower skins, while the second has a different spanwise variables distribution and mirrored thicknesses between suction side and pressure side during optimization (more details on design variables are presented in Sec. V). The third model is a preliminary composite structure made of balsa core and fiberglass plies based on Bak et al. [68] with simplifications. This composite model uses the same "mirrored" variables distribution as the second isotropic structural model. These three different models are optimized and compared in Sec. VI.B, but only the first is used for the coupled optimization studies presented in the following sections. In later developments, we aim at performing coupled optimization studies with a full-composite model and additional design

variables, including panel thickness, fiber angle, and ply fractional layup.

A snapshot of our preliminary structural model, with simplified geometry and isotropic shell elements, is shown in Fig. 2. Given aerodynamic and gravity loads as inputs, TACS is faster than the CFD solver by more than two orders of magnitude compared to the cheapest simulations with L3 aerodynamic mesh.

V. Problem Formulation

The multidisciplinary optimization problem we propose is aimed at improving the design of the turbine rotor. This design improvement takes into account both turbine rotor's efficiency in extracting power from the wind and its mass, which are the factors that ultimately drive the minimization of the cost of energy. A set of geometrical and structural variables are used to tailor the design of the blade and its steady-state aeroelastic response, exploiting the trade-offs between aerodynamic performance and weight reduction while satisfying nonlinear structural and performance constraints.

The generalized constrained optimization problem formulation is defined as:

$$\begin{aligned} &\min \ \mathbf{f}(\mathbf{x}) \\ &\text{w.r.t: } \mathbf{x}_{\min} \leqslant \mathbf{x} \leqslant \mathbf{x}_{\max} \\ &\text{s.t: } \mathbf{g}(\mathbf{x}) \leq 0 \end{aligned}$$

with $\mathbf{f}(\mathbf{x})$ a designer-defined objective function that quantifies the merit of the design, $\mathbf{x}$ is the full set of design variables, and $\mathbf{g}(\mathbf{x})$ are the nonlinear constraints. Note that in this formulation the upper and lower bounds of the design variables $\mathbf{x}_{\max}$ and $\mathbf{x}_{\min}$ are handled separately from other analysis-dependent constraints $\mathbf{g}(\mathbf{x})$. We discuss the project metrics $\mathbf{f}(\mathbf{x})$ described by Garcia-Sanz [9] in detail in Sec. V.D and focus on the description of the design variables $\mathbf{x}$ and constraints $\mathbf{g}(\mathbf{x})$ in the following paragraphs.

A. Design Variables:

Conventional design approaches are either limited in the number of high level parameters that can be directly used within an optimization, or require additional external iterations to update blade section polars or stiffness properties between optimization loops. One of the key advantages of the high-fidelity approach we are proposing is the possibility for the optimization algorithm (and the designer) to alter detailed features of the layout, such as airfoil shape or individual panel thicknesses, within a monolithic optimization loop. This both reduces human intervention in the loop, and avoids the discontinuities in the design space introduced by conventional multi-level strategies. In addition to the increased control on local variables for design and manufacturing considerations, the use of a representative 3D model enables a more accurate estimation of the mass of the system using an element-by-element calculation.

The realistic layout of the aerodynamic and structural meshes, coupled with FFD approach, enables a flexible and effective parametrization of geometry components that would otherwise be overlooked, approximated, or kept constant through the optimization. A snapshot of the aerodynamic model embedded in the FFD control box is illustrated in Fig. 3. Once we pre-process the FFD grid, we group control points and define their allowed displacement in *pyGeo*. This way, we can model both planform design variables and local airfoil shape deformations using the same geometry object. Pitch and twist variables are defined as rotations of the control sections of the FFD grid around a user-defined axis, while chord, thickness, and span are obtained by scaling the section size and spanwise location. The FFD control sections can also be displaced off the rotation plane to define other potential design variables such as pre-cone and pre-bend. Finally, the optimizer can handle the displacement of single control points to deform local airfoils. While these parametric variables are already implemented and available for use, the optimization studies we present are limited to the sole twist design variables to reduce problem complexity as we develop and test our models and tools.

As for the structural design variables, we split the structural mesh into 9 spanwise sections, with upper and lower skins further split into 4 chordwise sections, and assign an independent design variable to each of these structural panels (or "patches"). The structural parametrization of our preliminary model is shown in Fig. 4. TACS enables the optimizer to vary both the thickness of the panels and, when composite structures are considered, the fiber orientations of the baseline layup. For the cases presented below, we do not include ply angles as design variable and keep the fiber aligned with the spanwise axis - but they will be included in the composite model formulation in future works.

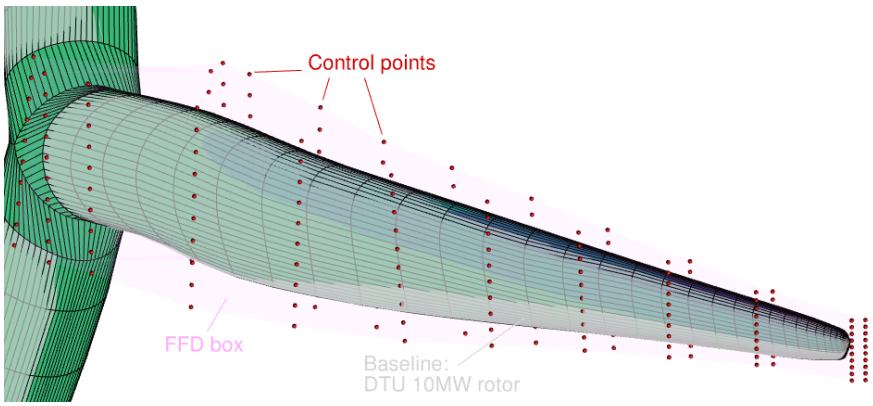

Fig. 3 Twisted aerodynamic mesh superimposed to the baseline configurations. The FFD control box is also highlighted.

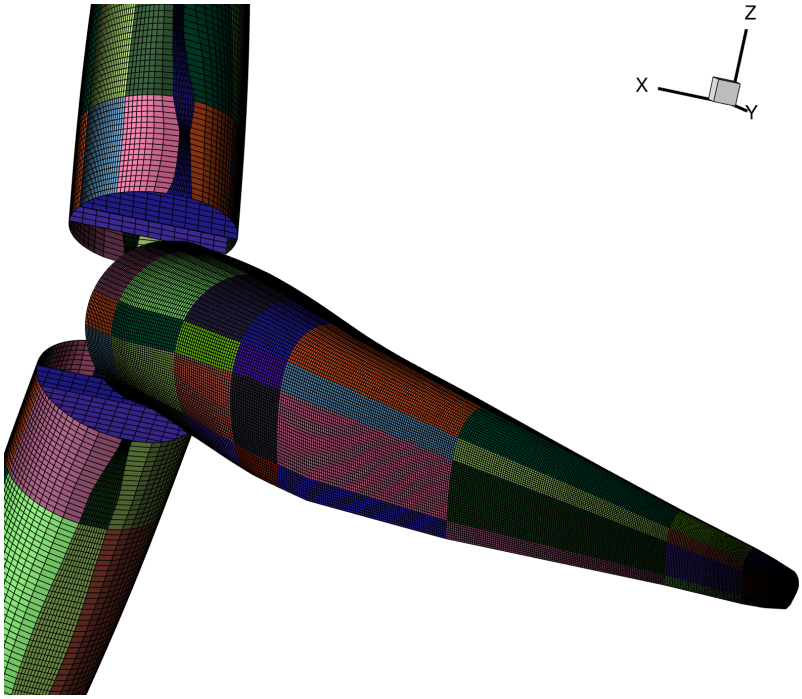

Fig. 4 Structural patches highlighted in randomized colors. Element thickness in each patch is defined by an independent design variable.

B. Constraints:

When only aerodynamic analysis tools are accessible during design, a typical way of introducing structural insights into aerodynamic optimizations is to enforce constraints on the thickness of the blade section or the bending moment to account for structural sizing considerations [11, 42]. The presence of a structural model makes it unnecessary to enforce these indirect constraints. TACS can be used to effectively size a feasible structure, taking into account local element-wise stresses. These element-wise constraints potentially challenge optimizations because a shell-by-shell approach dramatically increases the number of degrees of freedom of the problem. Moreover, the resulting function is expected to be non-smooth as critical elements can vary between successive optimization iterations, hindering optimization convergence. To implement these constraints efficiently and effectively in a gradient-based optimization context, we use a constraint aggregation technique described by Kennedy and Hicken [62]. These constraints are applied in order to group panels or blade assembly components, for example the upper and lower skins, and the spars. The same approach is used to aggregate the element displacement along the rotation axis and thus add a constraint on the maximum tip flapwise displacement, for sake of function smoothness. Under extreme load conditions, this displacement constraint accounts for the clearance between the deflected rotor and the tower. For the inflow condition that we are considering in this paper, the displacement constraint is used to define a reasonably-sized, pre-optimized initial configuration, and to maintain consistency in the subsequent optimizations. Finally, to ensure the optimizer does not allow abrupt thickness changes between adjacent panels, we enforce linear "adjacency" constraints in the structural model so that two structural patches next to each other have at most a 5 mm difference in thickness for the current problems.

C. Problem Summary

Tab. 1 lists the complete set of objective, variables, and constraints. The design metrics are discussed more in detail in Sec. V.D. From a numerical perspective, we normalize the torque and mass values with respect to the initial values. We observe how this normalization facilitates the convergence, while also enabling the combination of the two metrics in the same objective function. The displacement and torque constraints are also scaled by 10^{-3} and 10^{-2} respectively using a trial-and-error approach. We set the SNOPT convergence tolerances for both the feasibility and optimality conditions to 10^{-6}, which generally correspond to a reduction of more than three orders of magnitude from the initial design point.

Aerostructural Optimization			
	Name	Symbol	Qty
Objectives	Torque	M_1	1
	Mass	M_2	1
Design Variables	Panel thickness	$\mathbf{x_{st}}$	117
	Twist*	$\boldsymbol{\theta}$	7
Constraints	Max Stress	$\mathrm{KS}_{\sigma_{\max}} \leqslant 1$	3
	Tip Displacement	$\mathrm{KS}_{\mathrm{disp}} \leqslant 1$	1
	Torque†	$Q_x \geqslant Q_{x_{\mathrm{ref}}}$	1
	Adjacency constraints		318

Table 1 Optimization problem definition.
***: Only used in Sec. VI.D; †: Only used in Sec VI.C**

As explained in Sec. V.E, we consider a single-design-point optimization formulation in this paper, but the tools and the formulation above can be extended to multipoint optimization studies as done by Madsen et al. [11]. For the uncoupled structural optimization problems used for preliminary sizing (Sec. VI.B), the aerodynamic loads are evaluated running an MDA (with updated structural layout) outside the optimization loop, so that the loads are actually frozen during the single-discipline structural optimization itself. As we move on to coupled-system structural sizing

(Sec. VI.C), we first use M_2 (mass) as objective, while the torque is used as a constraint rather than part of the merit function. Finally, as we include geometric design variables in the formulation, we explore a weighted combination of M_1 and M_2 as objective functions to exploit the capabilities of our optimization framework.

D. Performance Metrics and Optimization Objective

Concerning the overall design objectives, there is a general consensus in academia and industry about using cost metrics as drivers for wind turbines and farms, often defined starting from a system-engineering approach [69–72]. In practical design terms, the cost of energy is driven by the power extraction of the turbine and the sum of investment and operating costs. Neglecting the market fluctuations and site-specific characteristics, the quality of a design is thus affected by both the pure aerodynamic efficiency under given conditions and the overall mass of the system. In this work, we use new metrics presented in [9] to measure the performance of our designs.

This new approach proposes to decouple the primary design drivers determining the levelized cost of energy (LCOE) from other environmental and economic factors. In its conventional definition, the LCOE is given by:

$$\text{LCOE} = \frac{\text{FCR} \times \text{CapEx} + \text{OpEx}}{\text{AEP}} \tag{1}$$

where OpEx stands for operation costs, AEP stands for the annual energy production, FCR stands for fixed charge rate, and CapEx stands for the capital expenditure. Assuming fixed OpEx, AEP is influenced by site-specific factors such as the wind probabilistic distribution, while CapEx is strongly dependent on the cost of steel, which in turn follows the market fluctuations.

The cost and performance components that determine the LCOE are split into two separate metrics in this work. Our focus is restricted to the technological primary design factors without considering these fluctuations. M_1 is introduced to assess the "air-to-electron" generation efficiency

$$M_1 = \frac{\sum_{k=1}^{N} P_e(k)}{\sum_{k=1}^{N} P_w(k)} \tag{2}$$

where the extracted electrical power, $P_e(k)$, and the total wind power, $P_w(k)$ are defined as

$$\begin{aligned} P_e(k) &= \frac{1}{2}\rho A_r(k) C_{p_{\max}}(k)\mu(k)V^3 \\ P_w(k) &= \frac{1}{2}\rho A_r(k) V^3 \end{aligned} \tag{3}$$

Here k is the turbine index, N is the total number of turbines under evaluation, V is the inflow velocity, A_r is the swept area, $C_{p_{\max}}$ is the maximum turbine power coefficient, and μ is the electromechanical loss coefficient.

The generalized cost of the farm is defined as the ratio of its swept area over its equivalent mass of steel (M_2):

$$M_2 = \frac{\sum_{k=1}^{N} A_r(k)}{\sum_{k=1}^{N} M_{eq}(k)}$$

where the equivalent mass of steel M_{eq}, and the component mass m_j are defined as:

$$\begin{aligned} M_{eq} &= \sum_{j=1}^{Z} m_j \\ m_j &= m_{cj} f_j \end{aligned}$$

with Z the total number of components, f_j the aggregated material, manufacturing, and installation factors and j the component index.

As we aim to analyze a single, isolated turbine rotor, these metrics are simplified to give:

$$M_1 = C_{p_{\max}} \tag{4}$$

$$M_2 = \frac{A_r}{M_{eq}} \tag{5}$$

where M_{eq} refers to the sole rotor mass for our optimization problem. The loss coefficient μ is neglected as the design optimization does not affect the gearbox and the generator. The M_1 function is not as comprehensive as the AEP metric to assess the "lifetime" power generation of a turbine, which must also take the probabilistic distribution of the wind resource into account. However, it is representative of the power production in region II. As we are not considering the peak torque for every configuration, we ultimately use $M_1 = C_P \propto Q_x$ evaluated at a chosen inflow velocity and TSR to compare the different designs in this paper.

Regardless of the number of inflow conditions considered, having two independent system metrics gives us the opportunity to compare different optimized designs with different weighted combinations of the metrics, for example:

$$f(\mathbf{x}) = aM_1 + bM_2 \tag{6}$$

with arbitrary non-negative parameters a and b where $a + b = 1$. Optimization study with this weighted objective is presented in Sec. VI.D.

E. Design Load Case

At the current development stage, we limit our optimization studies to a single design point to demonstrate the framework capabilities. For this reason, the "aerodynamic" objective for our optimizer is solely torque maximization at a prescribed inflow condition. We use the same reference below-rated-power design condition from the previous work on aerodynamic shape optimization [11] —namely a uniform inflow velocity V=8 m/s and a tip speed ratio TSR = 7.8. The same approach can be extended to a multipoint strategy [73, 74], averaging the performance of the turbine over a few selected inflow cases while using fatigue and extreme load conditions to size the internal structure of the rotor. Such an extension is discussed in [12] to overcome the shortcomings of the high-fidelity approach by including low-fidelity-informed load distributions in the optimization loop.

VI. Results

The analysis and optimization results discussed below represent the capabilities of the framework and the turbine modeling details as of November 2021. The model we use will be updated in future works to use finer aerodynamic meshes for better load estimation, a more refined spanwise discretization of the structural design variables to reflect the parametrization in [68], and most importantly the use of the anisotropic composite model in the coupled system optimizations. However, we consider the cases presented here a good indication of the tool's capability to complement the current state-of-the-art low-fidelity design approaches.

This section is organized as follows. In Sec. VI.A, we provide an example of the coupled aerostructural analysis and discuss the convergence properties and computational cost of our model. Structural optimization results are discussed in Sec. VI.B. The optimized structural layouts are used to define the baseline for the coupled-system optimization problems illustrated in Sec. VI.C, where we discuss the advantages of using the coupled aerostructural model over the single-discipline approach. In the last Sec. VI.D, we present a set of MDO studies using both twist and structural design variables, exploring the design space while optimizing for both torque maximization and mass reduction.

A. Multidisciplinary Analysis and Load-Displacement Transfer Verification

As the first high-fidelity aerostructural study of this paper, we briefly illustrate a multidisciplinary analysis (MDA) of the benchmark model. The analysis here uses the most refined aerodynamic mesh (L0) and the isotropic model used for coupled optimizations in Sec. VI.C- VI.D.

We use a Gauss–Seidel (GS) algorithm to converge the MDA, looping the loads and displacement between the aerodynamic and the structural modules respectively until the residuals in the two solvers are below a prescribed tolerance —10^{-3} for the results presented here. Depending on the convergence tolerance and the loading condition, the

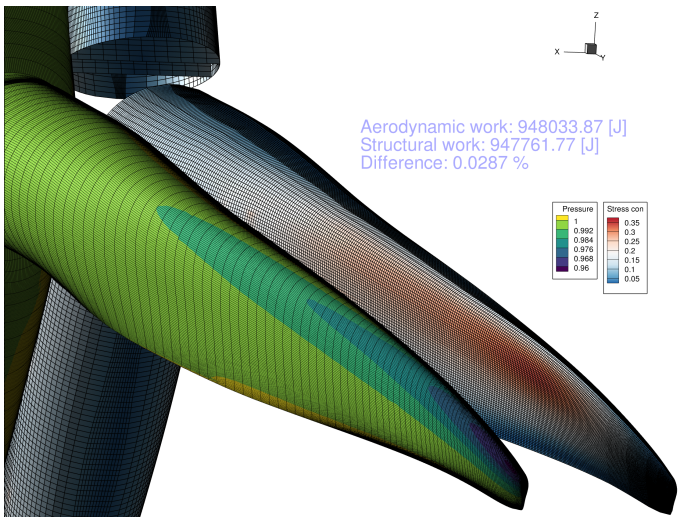

Fig. 5 Converged MDA on L0 aerodynamic mesh, with numerical error estimation of the load-displacement transfer scheme.

MDA converges between 6 and 25 iterations. Close to convergence, the cost of each iteration typically drops by one or two orders of magnitude. Overall, we typically observe an increase in the computational cost of approximately 80% compared to a stand-alone CFD solution. The efficient implementation of ADflow and TACS in MACH prevents a cost increase directly proportional to the number of GS iterations. Nevertheless, the increased analysis cost and the higher number of output functions with respect to the aerodynamic shape optimization studies in [11] makes these optimization studies numerically tractable only on High-Performance Computing clusters. The results reported in the following sections have been run on the Texas Advanced Computing Center's Stampede2 cluster and University of Michigan's Great Lakes cluster, using 1 (L3 mesh) or 2 (L2 mesh) Skylake nodes with 48 and 36 CPUs for each node on Stampede2 and Great Lakes respectively, with a wall time between 4 and 16 hours depending on the optimization cases.

For this analysis, we define an arbitrary input thickness distribution, which results in an oversized structure for the given inflow condition. Optimal structural sizing procedure and coupled system details are discussed from the next Sec. VI.B. The "stress con" variable shown in Fig. 5 is a material failure indicator, which is the local von Mises stress normalized by the yield strength. Without considering a safety factor, if this "stress con" value exceeds one, it indicates that material failure occurs. Because we consider a 1.5 safety factor for the failure indicator evaluation, the maximum allowable indicator is $\sigma_{\text{stress con}} = 1/1.5 = 0.667$. As shown in Fig. 5, the example MDA analysis results in a maximum value $\sigma_{\text{stress con}} \leqslant 0.38$. The measured tip displacement is 4.1 m and the loss of torque with respect to the rigid aerodynamic model of approximately 1.9%.

The load-displacement module used by MACH [10] is provably conservative and consistent. Nevertheless, we assess the numerical error affecting the turbine model used in this paper by comparing the work on the structural and aerodynamic models. The results of the dot product of the nodal displacement and force vectors as obtained by the two solvers on the final MDA iteration are reported in Fig. 5. We consider the relative error of 0.028% satisfying for the current set of models and optimization studies.

B. Uncoupled Structural Optimization

After we present the coupled aerostructural analysis capabilities, we demonstrate the optimization capabilities with uncoupled structural optimizations in this section. These structural optimization cases are relevant to discuss for two main reasons. On the one hand, we use this uncoupled, single-discipline approach to provide a reasonable initial structural layout for the coupled optimization problems presented later in this section. To make a fair comparison and to accelerate the computationally expensive coupled optimization, we need to use an initial thickness distribution that makes the rotor structurally feasible and lightweight; numerical optimization avoids the time-consuming and error-prone

task of manual tailoring. On the other hand, this approach highlights the benefits of including a full-blade FEM model within the preliminary design process even when the tightly-coupled model (and its derivatives) are not available. Although we discuss the benefits of the aerostructural coupling in the following sections, this loosely-coupled approach is still benefiting from the high-fidelity analysis coupled with a gradient-based optimizer. In addition to these points, we take the opportunity to compare the three different structural models (presented in Sec. V) and assess the impact of different design variables distribution and material properties on the final structural design.

For typical structural optimization studies, the structural layouts are optimized with the turbine rotor subject to a fixed aerodynamic load. This fixed aerodynamic load is computed by the CFD solver for a rigid blade before performing the optimization. However, performing a single optimization run with a fixed set of loads would largely miss the aeroelastic coupling between the structural and aerodynamic models, as a lighter and more flexible blade generally lead to a loss of steady-state aerodynamic performance, and a different load distribution more in general.

To ensure consistency between the optimized structure and the loads of the corresponding deflected rotor, we run a sequence of structural optimizations and aerostructural analyses instead. The initial aerodynamic load is obtained by running a full MDA on the arbitrarily-sized layout illustrated in Sec. VI.A. The optimizer minimizes the mass of the blades using this initial load while enforcing constraints on the aggregated stress and tip displacement. Once the structural optimization is completed, a new MDA is run using the intermediate optimized thickness distribution. The resulting loads from the new MDA are passed to the structural solver for new optimization. This loosely-coupled strategy converges in 4-6 MDA/optimization iterations, meaning that after that point any new optimization using an updated set of loads converges at the first (optimizer) iteration. The procedure is summarized in Algorithm 1 below.

Algorithm 1 Loosely-coupled structural optimization

Define initial layout
for $i \leftarrow 0$ to N **do** ▷ N=6 in this paper
1: Run MDA
2: Update aerodynamic input forces
3: Run structural optimization
4: Update structural layout
end for

Although this approach does not fully exploit the aeroelastic interactions of the coupled model, as discussed further in Sec. VI.C, it provides a valuable starting point for further optimizations while providing detailed insight on the "optimal" blade structural model.

	Mass $[kg]$	
Model	$d_{\text{tip}} = 2\ m$	$d_{\text{tip}} = 3\ m$
Isotropic	157 013.2	97 879.1
Isotropic (mirrored DVs)	160 026.3	101 244.5
Composite	196 326.7	114 865.2

Table 2 Mass of the optimized rotor models, as obtained via the loosely-coupled strategy in Algorithm 1.

Using the procedure illustrated above, we compare the optimized mass of our three structural models in Tab. 2. To quantify the impact of the arbitrarily-defined displacement constraints, we run two sets of optimization with $d_{\text{tip}} = 2\ m$ and $d_{\text{tip}} = 3\ m$ respectively. Given the selected inflow condition, these values represent rotor deflection limit at below-rated operating conditions and do not directly correspond to a rotor-tower clearance constraint, which needs to be evaluated under extreme load conditions. The impact of the stricter displacement constraint amounts to an average 63% increase in mass for the three models considered, with the composite model showing the highest sensitivity to the

displacement constraint with a 70% weight increase between the two optimized layouts. The composite model is also the heaviest of these optimal configurations in both cases. This is because it uses an overly conservative failure criterion, computed considering the weakest material at the outermost layer of the blade skins. Since balsa wood has a lower strength compared to fiberglass and aluminum, the optimized composite model is expected to be oversized with the current formulation. As a result, this does not necessarily imply that the composite design layout is the worse option, as broader manufacturing considerations are also included in LCOE and M_2 metrics for industrial applications. We also observe that enforcing the same thickness on upper and lower skins adds a weight penalty, which amounts to more than 3 tonnes when comparing the two "aluminum" configurations. Ultimately, it is worth noting how the inflow conditions we are optimizing the structure against are within ideal operating conditions. This approach leads to a lighter and more flexible blade than realistic industrial applications, where extreme loads are used for component sizing. Considering extreme and fatigue loads will drive up the thicknesses —at least for the aluminum structure.

In Fig. 6, we observe the impact of material properties, design variables, and constraints more closely. We report the thickness distribution for the three different models and $d_{\text{tip}} = 3\ m$ in Fig. 6(a). Because of the lower yield strength of the balsa core and the overly conservative failure criterion, the composite panel thicknesses are more than 3 mm higher over the entire blade with respect to the metallic isotropic configurations, requiring a different color map for clarity. All models present lower thickness close to the root, where the second moment of area of the blade sections with respect to edgewise bending is higher, increasing the local blade stiffness. Panel thickness is highest at mid span with the current parametrization. The optimizer reinforces the leading edge panels on the isotropic models, while focusing on the spar caps and a trailing edge section for the composite model. Again, the present structural sizing excludes any fatigue considerations, but the same methodology can be used with representative steady-state loads to include life-cycle considerations [12].

To isolate the effect of the tip displacement constraint, in Fig. 6(b) we show the optimization results for the same (isotropic) configuration with two different constraint values. The increase in thickness for the heavier, stiffer configuration (right) involves the entire blade, but it is more pronounced on the leading edge panels. The thickness of these elements increases by more than 7 mm while the root panels are on average 3 mm thicker. This reinforcement pattern is highlighted for tightly-coupled optimization studies in Sec. VI.C as well. Although this appears to apply to isotropic blades only, the results highlight a specific design pattern chosen by the optimizer to enforce user-defined design constraints. The same approach can be used on more detailed structural configurations to support design decisions while avoiding time-consuming manual iterations on the model: the optimization cases illustrated in this section converged in less than 2.6 CPU hours.

Presenting these results, the authors acknowledge that more design considerations have to be included in the model formulation of the composite model. In addition to the coarse spanwise discretization, the fiber angles of the layup are fixed to 0 degree with respect to the local spanwise axis. In future work, the optimizer will be given control of the ply fiber angles to leverage on the anisotropic properties of the fiberglass and balsa wood layup. For the optimizations in the following sections, we use the isotropic model without mirrored variables to give the optimizer a higher design freedom.

C. Tightly-coupled Optimal Structural Sizing

After having completed the preliminary sizing with the loosely-coupled methodology discussed in Sec. VI.B, we switch to the tightly-coupled approach to enable the optimizer to take full advantage of the high-fidelity coupled-physics model. We refer to this set of problems in terms of tightly-coupled optimal structural sizing because, although aerostructural design optimization is performed, we are using the sole structural variables while keeping the outer mold line unchanged. This is to differentiate these cases from those discussed in Sec. VI.D.

Note that we start from a more extreme structural layout than that presented in Table 2 —with a tip deflection of 5.64 m for the same inflow conditions. This makes the coupled optimization problem more challenging as the initial structure is closer to the prescribed stress limit, thus limiting further mass reduction. The use of the coupled model enables the inclusion of aerodynamic performance metrics in the optimization formulation. In the problems presented in this section, we enforce a torque constraint in addition to the stress and displacement constraints. More specifically, we enforce the torque output to remain the same as the baseline while allowing up to 5% tip displacement increase.

The initial and final layouts of the case we just presented are illustrated in Fig. 7. The optimizer rearranges the internal thickness distribution to reduce the total rotor mass by 9.1% compared to the uncoupled optimization result. The changes in panel thickness occur over the entire span of the blade. The optimized structure has a more homogeneous

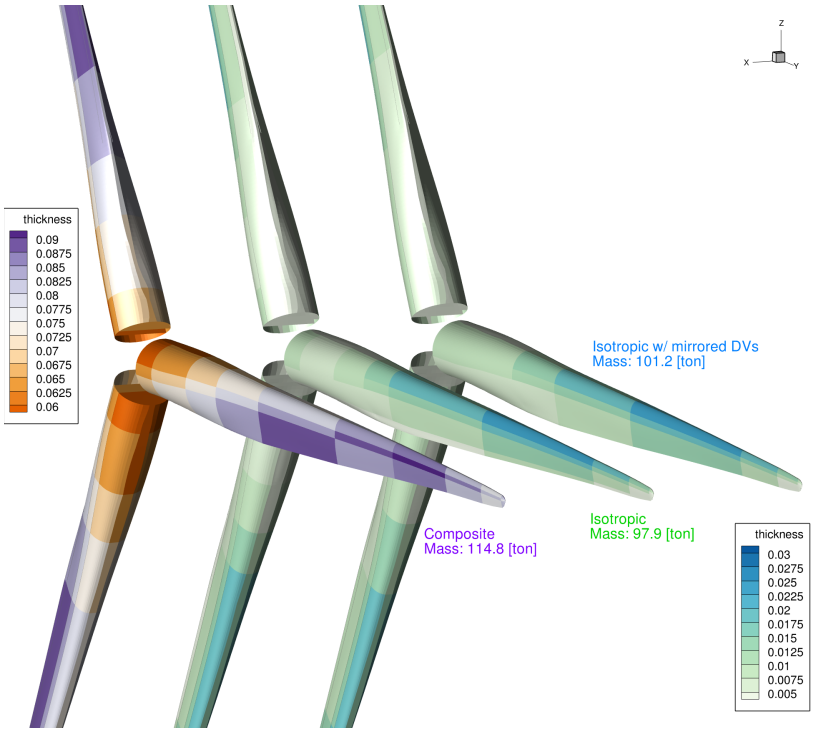

(a) The three structural models, optimized with maximum $d_{\text{tip}} = 3m$

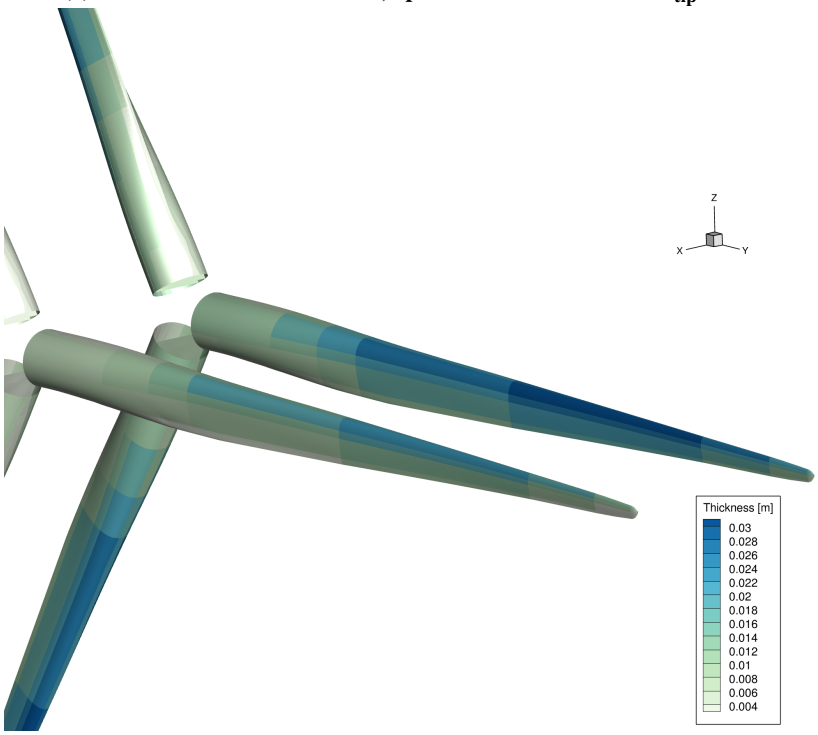

(b) Isotropic model with displacement constraint set to $d_{\text{tip}} = 3m$ (left) and $d_{\text{tip}} = 2m$ (right)

Fig. 6 Thickness distribution for the composite and isotropic models, optimized using single-discipline optimization with updated aerodynamic loads.

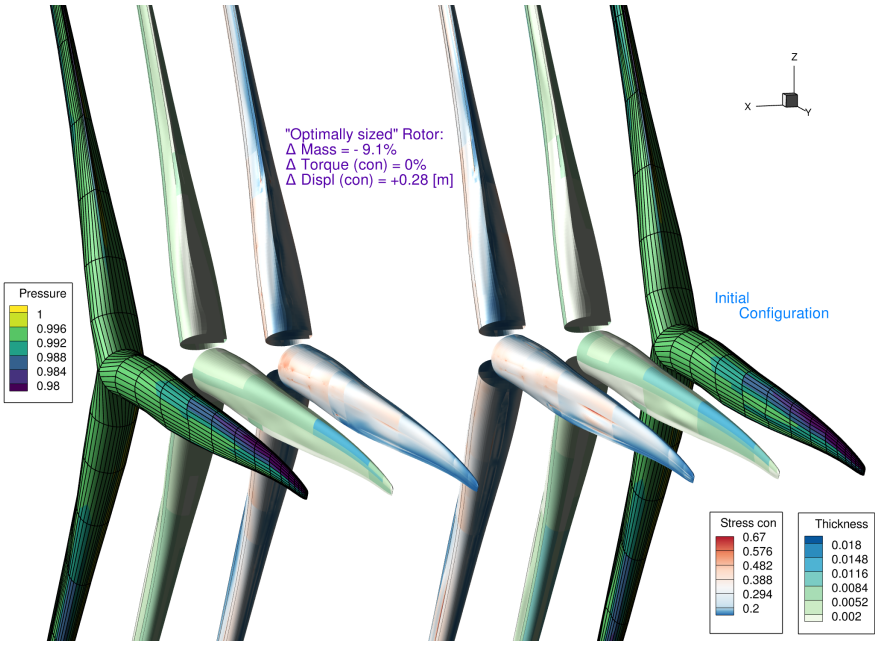

Fig. 7 Pressure, thickness, and stress distribution of the baseline and optimized rotors, using the tightly-coupled model and the sole structural design variables. The optimized layout has the same torque of the baseline and an 5% increase in tip displacement, and a mass reduction of 9.1%.

thickness at the root section, with the leading and trailing edge panels being now within 1 *mm* from each other instead of the initial 4 *mm* difference. The optimizer in particular reduces the thickness on the front section and reinforces the trailing edge panels. These latter panels are increasing in thickness more gradually from root to tip on the optimized design, instead of the more abrupt thickness increase observed in the baseline layout. At both mid span and the tip of the blade, the leading edge panel is also reduced by 1.5 *mm*, including the reinforced leading edge section in the darker blue color in Fig. 7. These adjustments over the entire span lead to a reduction of the overall mass of the rotor by 4.5 tonnes.

The stress distribution over the blade is also altered in the final layout. The optimized layout presents higher stresses at the root when compared to the starting point, while the load concentrations around mid-span are reduced as the thickness difference between the leading edge panels and the spar cap is reduced. It is interesting to note from the trends in Fig. 8 how for this set of constraints, the lower skin is the critically stressed section, while the spars and the upper skin end up having a lower aggregated stress indicator value on the optimal design. Both the torque and displacement constraints are active at the optimum. The optimizer first reaches the maximum allowed displacement bound, and then rearranges the thickness distribution to match the minimum torque value.

Despite the updates of the aerodynamic load between structural optimizations described in Sec. VI.B, the initial evaluation using the coupled system has an aggregated stress approximately 5% lower than the prescribed value. The optimizer is thus able to reduce the total mass by taking advantage of this margin. This is partially explained by the use of a coarsened structural mesh (for cost and optimization robustness reasons) for the coupled optimization runs instead of the finer one used for preliminary structural sizing, which might reduce stress concentrations on critical elements of the blade. However, we observed how regardless of the specific cases presented in this section, the coupled optimization consistently improves the layout obtained via uncoupled optimization. Future works will investigate this optimization behavior more in detail.

The mass reduction discussed in the case above is also partially justified by the 5% increase in tip displacement. This increase is less than 30 cm. However, the total mass reduction is not fully attributed to this relaxed constraint as well: the coupled approach itself brings quantifiable sizing benefits with respect to the single-discipline preliminary sizing. We will discuss the intrinsic sizing benefits in the following paragraph. Even after considering the points above, this example illustrates how the optimizer is able to exploit the coupled effects affecting the steady aeroelastic response of the

blade, converging to a different and lighter configuration than the design obtained using the loosely-coupled approach.

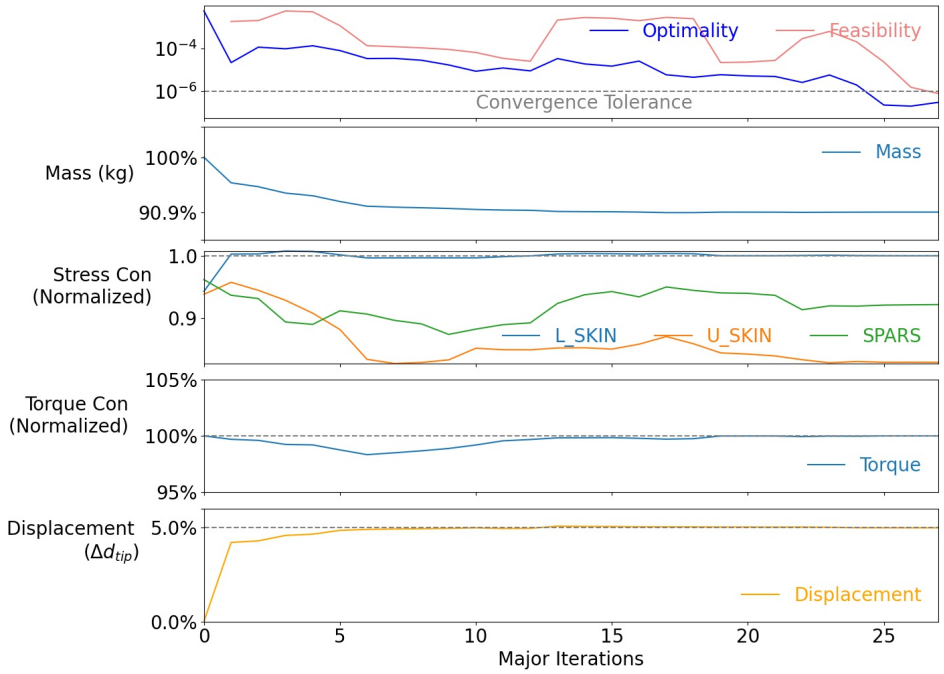

Fig. 8 Optimization convergence trends for the optimization shown in Fig. 7

As shown by Fig. 8, the optimizer converges below the 10^{-6} tolerance in 27 major iterations, corresponding to 120.5 CPU hours. However, the computational cost is problem-dependent, with some of the cases presented requiring more than 100 iterations and 500 CPU hours. In some instances, the optimizer was not able to fully converge to the prescribed tolerance for the optimality condition, potentially falling short of further mass reduction. Nevertheless, the feasibility condition is obtained for all the cases discussed, ensuring that the nonlinear constraints are not violated, and the final design is within the prescribed stress, displacement, and torque values.

The advantage of the coupled-system optimization approach and its sensitivity to nonlinear torque and displacement constraints is outlined in Fig. 9 over a broader set of optimization problems. Δd_{tip} is defined as the increase (in percentage) of the tip displacement with respect to the baseline value of 5.46 m. We use the same problem formulation discussed above and explore this design space by varying the prescribed constraint value, ranging from 100% to 85% of initial torque values, and from 0% to 15% of tip displacement increase with respect to the initial layout. The optimization results shown in Fig. 7- 8 correspond to the rightmost point in the orange line in Fig. 9.

There are a few key insights to unpack in this figure. In the first place, the results marked as $\Delta d_{\text{tip}} = 0\%$ highlight the advantage of using the coupled model rather than just the single-discipline approach used in Sec. VI.B. The rightmost point of this set refers to an optimization where we maintain the same displacement and torque as the initial configuration, and are nevertheless able to reduce the total mass (expressed by the normalized M_2 metric) by 4.1%. As hinted earlier in this section, when the coupled model is used the optimizer can take full advantage of the reciprocal effects of the aerodynamic loads on the stress distribution and, vice versa, of the structural displacements on the aerodynamic loads.

Secondly, the availability of the torque constraint allows us to perform structural sizing while practically enforcing a prescribed torque value (normalized M_1 metric) and obtain the lightest blade possible with the given parametrization. In the range we are investigating, we observe a linear relationship between the rotor torque and the available mass decrease. The mass decreases amounts up to 7.8% for a 15% reduction of the initial torque. This trend appears to be loosely related to the prescribed displacement constraint. The final mass difference between the 100% and the 85% torque cases amounts to 3.7% for $\Delta d_{\text{tip}} = 0\%$ and 5.3% for $\Delta d_{\text{tip}} = 15\%$, showing that the optimizer can also take advantage of the coupled effects of simultaneously relaxing the two constraints.

Looking at the general trends, the optimal designs obtained with this formulation are more sensitive to the

displacement constraint than to the overall torque. This can be explained with the same considerations reported in Sec. VI.B. For the prescribed flapwise tip displacement, the optimizer tends to reinforce the outer section of the blades by thickening the panels by up to 14 *mm*.

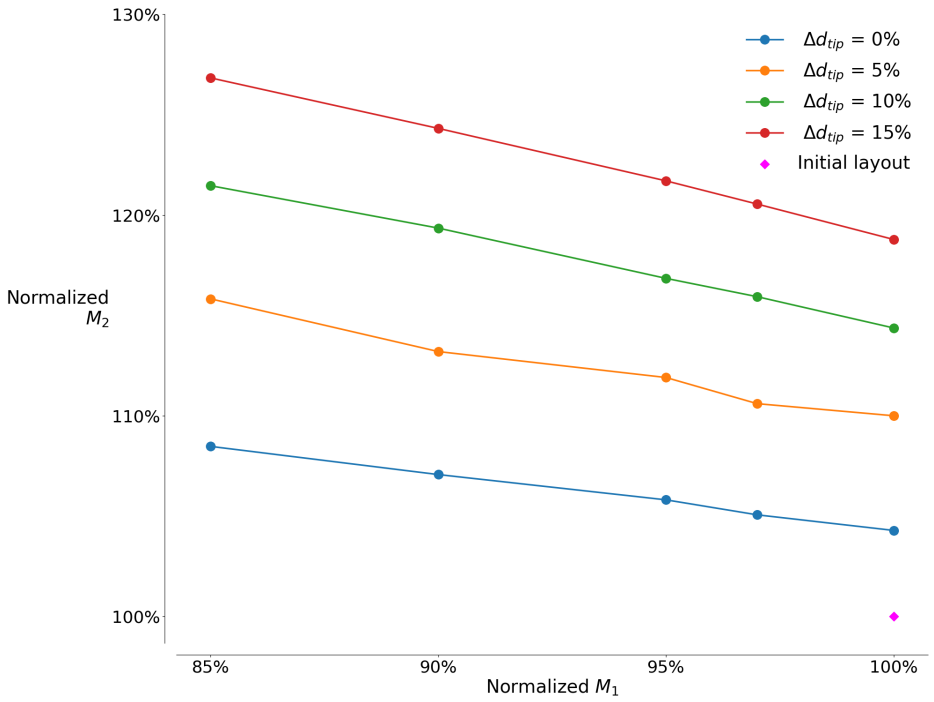

Fig. 9 Design space exploration for optimally-sized rotors using M_1 (torque) and M_2 (inverse of the mass) metrics. Different Pareto fronts refer to different optimization sets with different maximum tip displacement constraint.

D. MDO with Structural and Geometric Variables

As a final study, we perform a multidisciplinary design optimization of the reference turbine using both structural and geometrical design variables, namely allowing the optimizer to change the twist distribution. Considering this additional set of design variables, we include the rotor torque in the objective and explore the design trade-offs when mass and torque are given different weight within the objective —as described in Sec. V. For this set of problems, we switch to the more expensive but more accurate L2 mesh to better capture the effects of twist variation on the aerodynamic load. We use a less strict displacement constraint than the case in Sec. VI.C, allowing a maximum tip displacement of 10% of the baseline reference value.

A set of optimizations with varying objective function is presented in Fig. 10, using again M_1 and M_2 metrics normalized with respect to the baseline MDA. We include two cases that use a subset of design variables. The point labeled "Mass min (struct only)" refers to an optimization with the same formulation as those presented in Sec. VI.C using L3 meshes: it is a torque-constrained mass minimization problem using the sole structural variables. With this aerodynamic mesh and set of constraints, the optimizer reduces the mass by 11.9% (M_2=+13.6%). On the other hand, the "Torque max (twist only)" point refers to a torque maximization problem that retains the initial thickness distribution of the baseline, loosely-coupled optimum and only uses twist as design variables. The formulation is identical to what was used for aerodynamic shape optimization problems in [11], this time applied to the coupled aerostructural model with the addition of stress constraints. These constraints are added to ensure that the optimized layout is still structurally feasible without changes in the thickness distribution. The optimizer increases the torque output by 6.8% as the stress on the lower skin approaches the maximum allowable value.

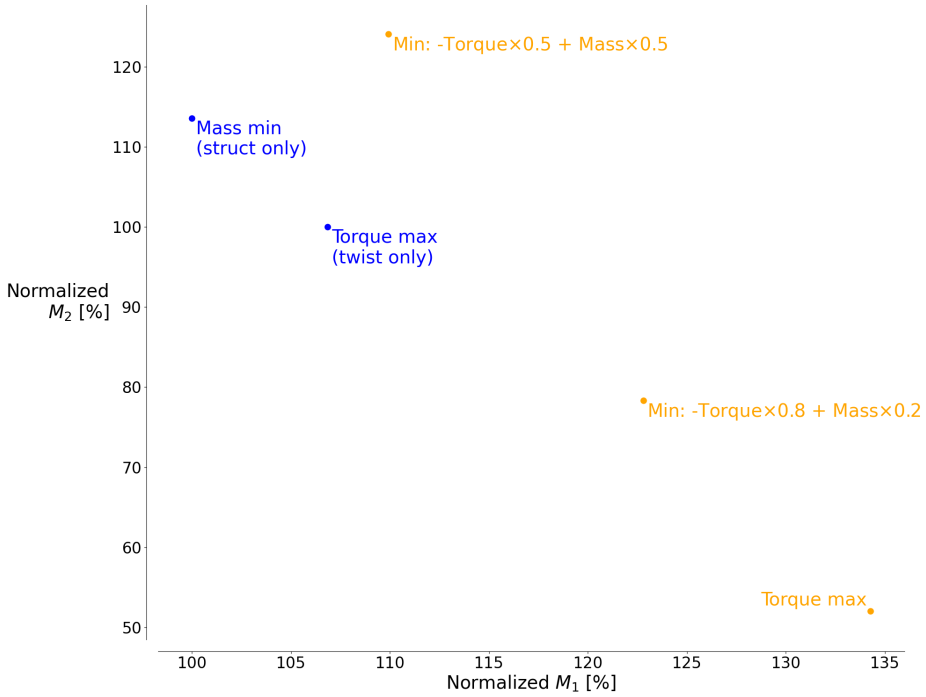

Fig. 10 Multidisciplinary design optimizations using a weighted sum of M_1 (Torque) and M_2 (inverse of the mass) metrics as objective. Results in orange use the full set of structural and twist design variables.

At the bottom right of the plot, the "Torque max" refers to optimization with the same formulation of the latter, this time including both twist and structural design variables. The possibility to modify the internal layout leads to a torque increase of 34.3% at this inflow condition. The higher panel thickness has two main effects on the design. On the one hand, the optimizer can reinforce the stress-critical panels, thus enabling a more aggressive twist increase over the blade and higher loads without incurring structural failure. Secondly, the optimizer can reinforce the mid-span section to reduce the tip displacement and so minimize the torque loss due to the flexibility of the rotor. However, the resulting rotor mass is increased by 92% with respect to the baseline layout, suggesting that this design would be sub-optimal from an LCOE perspective. The sizing of the structure is ultimately driven by extreme loads that are not considered in this study, but this problem highlights how the selection of the objective function and design variables leads to different design outcomes.

Having investigated these corner cases, we run an optimization problem where the (normalized) torque and weight are equally weighted in the objective function - see "-Torque× 0.5 + Mass× 0.5" in Fig. 10. Despite this case not reaching full prescribed convergence, the optimized design has its M_2 10.5% higher than the "Mass min" configuration and its M_1 3.1% higher than the"Torque max" configuration, meaning that the optimizer is simultaneously improving both metrics and taking advantage of the coupled effects of thickness and twist distribution. This demonstrates how the high-fidelity optimization approach we propose enables rotor design improvements considering the aerodynamic efficiency and the mass simultaneously while taking into account the steady aeroelastic response of the blade and its structural feasibility. We discuss this optimized design in more detail later in this section.

The selection of the objective weights is not trivial. Although the designer has a high-level intuition on which metric to privilege in the optimization, large differences in these coefficients can lead to a net objective improvement even if the efficiency decreases or, conversely, the total mass increases. The "-Torque×0.8 + Mass×0.2" case refers to a problem where the torque is given four times more relevance than the mass in the objective. Despite the mass minimization still being part of the optimization goal, the increase in torque overcomes the mass addition, leading to a final rotor design that has 22.8% higher torque but also weights 27.6% more than the baseline configuration. These non-linearities between the objective weights and the final metrics are indeed hard to predict. Considerations on the

LCOE and manufacturer-dependent cost models could drive the selection of these weights in industrial applications. The exploration of the Pareto front provides the engineers with useful insight on the sensitivity of the optimized layouts to such cost and optimization objective considerations. The results in this section ultimately show how higher design freedom enables the optimizer to generate more extreme layouts, lighter and more efficient at the same time. Additional investigations will be necessary to analyze the design space more in detail and complete the outline of the Pareto front. In future developments, we aim at performing such detailed analysis while also including additional geometric design variables.

In conclusion, in Fig. 11 we take a deeper look at the "dominant" optimum "-Torque× 0.5 + Mass× 0.5" compared to the other weighted-objective "-Torque×0.8 + Mass×0.2" optimization from Fig. 10. The latter case, on the left side of the figure, has lower tip deflection (6.7 m versus 8.1 m) and higher thickness over the entire blade, in particular on the leading edge panels discussed in Sec. VI.B. For the "-Torque×0.8 + Mass×0.2" optimum the thicker leading edge panel is almost double than its counterpart on the other case (15.3 mm vs 8.4 mm). The final design for this case has a higher torque increase with respect to the baseline case, but outweighs the other optimal layout by 24.7 tonnes. Using an objective that equally weighs the mass and torque in the objective leads to a less efficient (with respect to the "-Torque×0.8 + Mass×0.2" case) but lighter design. For this reason, the stress concentrations are higher on this configuration, and both the stress and displacement constraints are active at the optimum.

Identifying the best design among these two is a design decision that involves broader manufacturing, sizing, and site-specific considerations. Nevertheless, we demonstrate how our tool can be used to explore this complex and high-degree-of-freedom design space and identify design trends while taking into account coupled aeroelastic effects.

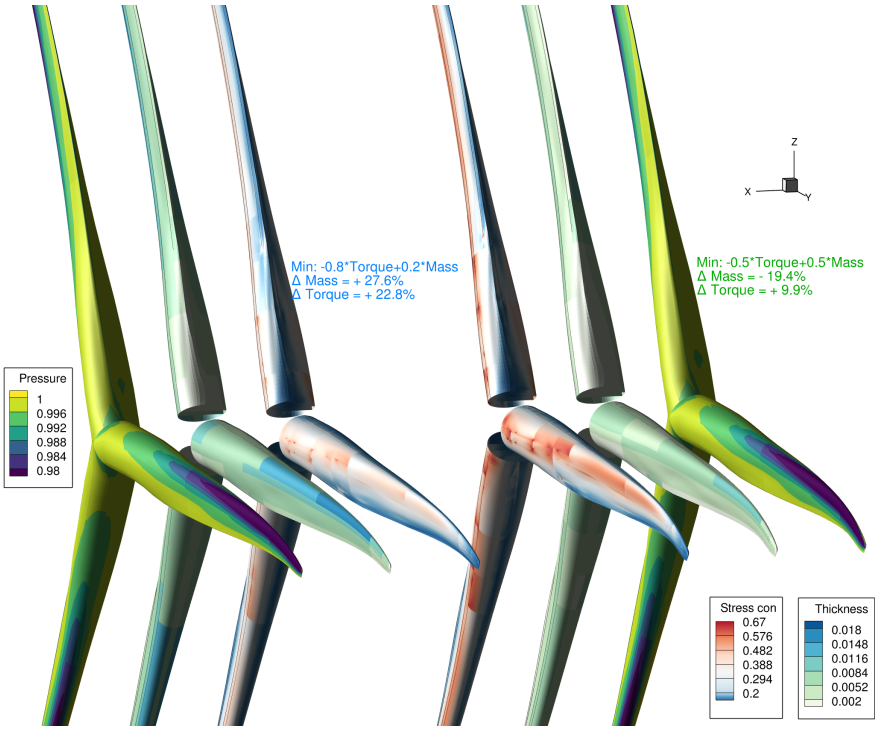

Fig. 11 MDO using both structural and geometric design variables. The objective for this case is an equally-weighted average of normalized mass and torque.

VII. Conclusions

In this work, we apply our high-fidelity aerostructural optimization framework, MACH, to improve the performance of the rotor of the DTU 10MW benchmark wind turbine model. We first introduce the research problem and discuss

how our work complements more conventional design approaches. The increase in computational cost due to the CFD and FEM tools is justified by a higher model and physics resolution. Moreover, the use of 3D models extend the design freedom within the optimization context, as the optimizer can simultaneously modify the internal structural layout and the outer mold line of the rotor while exploiting steady-state aeroelastic coupling.

The efficient implementation of MACH enables us to perform gradient-based optimization with more than 100 design variables while including a set of structural and aerodynamic performance constraints. The optimization cases we present focus on both mass minimization, torque maximization, and a combination of these two objectives. We limit our investigations to a single steady-state inflow case, with the sole panel thicknesses and spanwise twist distribution as design variables. A broader set of design variables will be included in future works. Moreover, the approach hereby presented can be extended to include multiple inflow conditions and, as done in another work presented at SciTech 2022, can include extreme and fatigue load cases as extracted via conventional design tools.

In the result section, we first illustrate our preliminary sizing strategy using a loosely-coupled structural optimization approach. We compare the final rotor weight of three structural models and assess the impact of the displacement constraint on the internal thickness distribution and the overall mass. This optimization approach is faster and less implementation-heavy than using a fully-coupled approach, while providing detailed insight on internal structure design trends. However, when we use the layouts obtained with this approach as the starting point for mass minimization problems using the tightly-coupled aerostructural model, we show how the latter strategy can leverage the aeroelastic interactions on the blade to further reduce the total weight of the rotor. For these problems, we use the sole structural variables and enforce stress, displacement, and torque constraints. Finally, we include twist variables in the optimization and compare the results of different optimizations with different objective functions. We show how the optimizer can simultaneously reduce the mass and increase the torque of the baseline configuration when both metrics are equally weighted in the objective function. Moreover, we partially explore the design space, showing how this problem formulation can be used by designers to assess the implications of different cost-of-energy model assumptions on the final layout.

The results in this paper highlight how high-fidelity aerostructural optimization can be leveraged to identify design patterns and detailed trends to complement conventional analysis tools for large wind turbines. The authors are working to improve the reference model and formulate more complex and realistic optimization problems to fully demonstrate the feasibility and effectiveness of this approach. The application of tools as MACH early in the design process could lead to more efficient and lighter rotors while reducing design costs, reducing the number of manual design iterations at a preliminary and detailed design level.

Acknowledgments

This research is supported by the Department of Energy (DOE) Advanced Research Projects Agency-Energy (ARPA-E) Program award DE-AR0001186 entitled "Computationally Efficient Control Co-Design Optimization Framework with Mixed-Fidelity Fluid and Structure Analysis." The authors thank DOE ARPA-E Aerodynamic Turbines Lighter and Afloat with Nautical Technologies and Integrated Servo-control (ATLANTIS) Program led by Dr. Mario Garcia-Sanz. Special thanks to the entire ATLANTIS Team for their support.

This research was supported in part through computational resources and services provided by Advanced Research Computing at the University of Michigan, Ann Arbor. The authors also made extensive use of the Texas Advanced Computing Center (TACC) Stampede2 High Performance Computing system via the Extreme Science and Engineering Discovery Environment (XSEDE), which is supported by the National Science Foundation grant number ACI-1548562.

References

[1] Masson-Delmotte, V., Zhai, P., Pörtner, H.-O., Roberts, D., Skea, J., Shukla, P. R., Pirani, A., Moufouma-Okia, W., Péan, C., Pidcock, R., et al., "Global warming of 1.5 C. An IPCC Special Report on the impacts of global warming of 1.5°C above pre-industrial levels and related global greenhouse gas emission pathways, in the context of strengthening the global response to the threat of climate change, sustainable development, and efforts to eradicate poverty." Tech. rep., Intergovernmental Panel on Climate Change (IPCC), 2018. URL https://www.ipcc.ch/site/assets/uploads/sites/2/2019/06/SR15_Full_Report_High_Res.pdf.

[2] Cozzi, L., Gül, T., and Bouckaert, S., "Net Zero by 2050 - A Roadmap for the Global Energy Sector," Tech. rep., IEA, May 2021.

[3] Musial, W., Heimiller, D., Beiter, P., Scott, G., and Draxl, C., "2016 Offshore Wind Energy Resource Assessment for the United States," Tech. Rep. NREL/TP-5000-66599, National Renewable Energy Laboratory, 2016. URL http://www.nrel.gov/docs/fy16osti/66599.pdf.

[4] Prakash, G., and Anuta, H., "Future of Wind: Deployment, investment, technology, grid integration and socio-economic aspects," Tech. Rep. NREL/TP-5000-66599, International Renewable Energy Agency (IRENA), 2019. URL https://www.irena.org/publications/2019/Oct/Future-of-wind.

[5] Hau, E., *Wind Turbines — Fundamentals, Technologies, Application, Economics*, 2nd ed., Springer, 2006.

[6] Bottasso, C. L., Bortolotti, P., Croce, A., and Gualdoni, F., "Integrated aero-structural optimization of wind turbines," *Multibody System Dynamics*, Vol. 38, No. 4, 2016, pp. 317–344.

[7] Barrett, R., and Ning, A., "Integrated free-form method for aerostructural optimization of wind turbine blades," *Wind Energy*, Vol. 21, No. 8, 2018, pp. 663–675. doi:10.1002/we.2186.

[8] Martins, J. R. R. A., and Lambe, A. B., "Multidisciplinary Design Optimization: A Survey of Architectures," *AIAA Journal*, Vol. 51, No. 9, 2013, pp. 2049–2075. doi:10.2514/1.J051895.

[9] Garcia-Sanz, M., "A Metric Space with LCOE Isolines for Research Guidance in wind and hydrokinetic energy systems," *Wind Energy*, Vol. 23, No. 2, 2020, pp. 291–311. doi:https://doi.org/10.1002/we.2429, URL https://onlinelibrary.wiley.com/doi/abs/10.1002/we.2429.

[10] Kenway, G. K. W., Kennedy, G. J., and Martins, J. R. R. A., "Scalable Parallel Approach for High-Fidelity Steady-State Aeroelastic Analysis and Adjoint Derivative Computations," *AIAA Journal*, Vol. 52, No. 5, 2014, pp. 935–951. doi:10.2514/1.J052255.

[11] Madsen, M. H. A., Zahle, F., Sørensen, N. N., and Martins, J. R. R. A., "Multipoint high-fidelity CFD-based aerodynamic shape optimization of a 10 MW wind turbine," *Wind Energy Science*, Vol. 4, 2019, pp. 163–192. doi:10.5194/wes-4-163-2019.

[12] Caprace, D.-G., Cardoza, A., Nakamoto, T., Ning, A., Mangano, M., He, S., and Martins, J. R. R. A., "Incorporating High Fidelity Aero-Structural Analyses in Wind Turbine Rotor Optimization," *Abstract submitted for AIAA SciTech 2022*, 2022.

[13] "OpenFAST v2.6.0," , May 14, 2021. URL https://github.com/OpenFAST/openfast.

[14] Zahle, F., Tibaldi, C., Pavese, C., McWilliam, M. K., Blasques, J. P. A. A., and Hansen, M. H., "Design of an Aeroelastically Tailored 10 MW Wind Turbine Rotor," *Journal of Physics: Conference Series*, Vol. 753, No. 6, 2016, p. 062008.

[15] Scott, S., Macquart, T., Rodriguez, C., Greaves, P., McKeever, P., Weaver, P., and Pirrera, A., "Preliminary validation of ATOM: an aero-servo-elastic design tool for next generation wind turbines," *Journal of Physics: Conference Series*, Vol. 1222, IOP Publishing, 2019, p. 012012.

[16] del Carre, A., Muñoz-Simón, A., Goizueta, N., and Palacios, R., "SHARPy: A dynamic aeroelastic simulation toolbox for very flexible aircraft and wind turbines," *Journal of Open Source Software*, Vol. 4, No. 44, 2019, p. 1885.

[17] Marten, D., Wendler, J., Pechlivanoglou, G., Nayeri, C. N., and Paschereit, C. O., "QBLADE: an open source tool for design and simulation of horizontal and vertical axis wind turbines," *Int. J. Emerging Technol. Adv. Eng*, Vol. 3, No. 3, 2013, pp. 264–269.

[18] Leimeister, M., Kolios, A., and Collu, M., "Development of a Framework for Wind Turbine Design and Optimization," *Modelling*, Vol. 2, No. 1, 2021, pp. 105–128. doi:10.3390/modelling2010006, URL https://www.mdpi.com/2673-3951/2/1/6.

[19] Ramos-García, N., Sessarego, M., and Horcas, S. G., "Aero-hydro-servo-elastic coupling of a multi-body finite-element solver and a multi-fidelity vortex method," *Wind Energy*, Vol. 24, No. 5, 2021, pp. 481–501.

[20] Heinz, J. C., Sørensen, N. N., and Zahle, F., "Fluid–structure interaction computations for geometrically resolved rotor simulations using CFD," *Wind Energy*, Vol. 19, No. 12, 2016, pp. 2205–2221. doi:https://doi.org/10.1002/we.1976, URL https://onlinelibrary.wiley.com/doi/abs/10.1002/we.1976.

[21] Saverin, J., Peukert, J., Marten, D., Pechlivanoglou, G., Paschereit, C. O., and Greenblatt, D., "Aeroelastic simulation of multi-MW wind turbines using a free vortex model coupled to a geometrically exact beam model," *Journal of Physics: Conference Series*, Vol. 753, 2016, p. 082015. doi:10.1088/1742-6596/753/8/082015, URL https://doi.org/10.1088/1742-6596/753/8/082015.

[22] Lee, K., Huque, Z., Kommalapati, R., and Han, S.-E., "Fluid-structure interaction analysis of NREL phase VI wind turbine: Aerodynamic force evaluation and structural analysis using FSI analysis," *Renewable Energy*, Vol. 113, 2017, pp. 512–531. doi:https://doi.org/10.1016/j.renene.2017.02.071, URL https://www.sciencedirect.com/science/article/pii/S096014811730157X.

[23] Wainwright, T. R., Poole, D. J., Allen, C. B., Appa, J., and Darbyshire, O., "High Fidelity Aero-Structural Simulation of Occluded Wind Turbine Blades," *AIAA Scitech 2021 Forum*, ????, pp. –. doi:10.2514/6.2021-0950, URL https://arc.aiaa.org/doi/abs/10.2514/6.2021-0950.

[24] Cheng, P., Huang, Y., and Wan, D., "A numerical model for fully coupled aero-hydrodynamic analysis of floating offshore wind turbine," *Ocean Engineering*, Vol. 173, 2019, pp. 183–196. doi:https://doi.org/10.1016/j.oceaneng.2018.12.021, URL https://www.sciencedirect.com/science/article/pii/S0029801818314124.

[25] Gray, J. S., Hearn, T., Moore, K., Hwang, J. T., Martins, J. R. R. A., and Ning, A., "Automatic Evaluation of Multidisciplinary Derivatives Using a Graph-Based Problem Formulation in OpenMDAO," *Proceedings of the 15th AIAA/ISSMO Multidisciplinary Analysis and Optimization Conference*, Atlanta, GA, 2014. doi:10.2514/6.2014-2042.

[26] Ning, A., and Petch, D., "Integrated design of downwind land-based wind turbines using analytic gradients," *Wind Energy*, Vol. 19, No. 12, 2016, pp. 2137–2152. doi:10.1002/we.1972.

[27] Ingersoll, B., and Ning, A., "Efficient incorporation of fatigue damage constraints in wind turbine blade optimization," *Wind Energy*, Vol. 23, No. 4, 2020, pp. 1063–1076. doi:https://doi.org/10.1002/we.2473, URL https://onlinelibrary.wiley.com/doi/abs/10.1002/we.2473.

[28] Bottasso, C. L., Campagnolo, F., and Croce, A., "Multi-disciplinary constrained optimization of wind turbines," *Multibody System Dynamics*, Vol. 27, No. 1, 2012, pp. 21–53.

[29] Bortolotti, P., Bottasso, C. L., and Croce, A., "Combined preliminary–detailed design of wind turbines," *Wind Energy Science*, Vol. 1, No. 1, 2016, pp. 71–88. doi:10.5194/wes-1-71-2016, URL https://wes.copernicus.org/articles/1/71/2016/.

[30] Scott, S., Greaves, P., Weaver, P. M., Pirrera, A., and Macquart, T., "Efficient structural optimisation of a 20 MW wind turbine blade," *Journal of Physics: Conference Series*, Vol. 1618, IOP Publishing, 2020, p. 042025.

[31] McWilliam, M. K., Zahle, F., Dicholkar, A., Verelst, D., and Kim, T., "Optimal aero-elastic design of a rotor with bend-twist coupling," *Journal of Physics: Conference Series*, Vol. 1037, IOP Publishing, 2018, p. 042009.

[32] Horcas, S. G., Debrabandere, F., Tartinville, B., Hirsch, C., and Coussement, G., "CFD study of DTU 10 MW RWT aeroelasticity and rotor-tower interactions," *MARE-WINT*, Springer, Cham, 2016, pp. 309–334.

[33] Martins, J. R. R. A., and Ning, A., *Engineering Design Optimization*, Cambridge University Press, 2021. URL https://mdobook.github.io.

[34] Kenway, G. K. W., and Martins, J. R. R. A., "Multipoint High-Fidelity Aerostructural Optimization of a Transport Aircraft Configuration," *Journal of Aircraft*, Vol. 51, No. 1, 2014, pp. 144–160. doi:10.2514/1.C032150.

[35] Brooks, T. R., Martins, J. R. R. A., and Kennedy, G. J., "High-fidelity Aerostructural Optimization of Tow-steered Composite Wings," *Journal of Fluids and Structures*, Vol. 88, 2019, pp. 122–147. doi:10.1016/j.jfluidstructs.2019.04.005.

[36] Liao, Y., Martins, J. R. R. A., and Young, Y. L., "3-D High-Fidelity Hydrostructural Optimization of Cavitation-Free Composite Lifting Surfaces," *Composite Structures*, 2021. (In press).

[37] Lambe, A. B., and Martins, J. R. R. A., "Extensions to the Design Structure Matrix for the Description of Multidisciplinary Design, Analysis, and Optimization Processes," *Structural and Multidisciplinary Optimization*, Vol. 46, 2012, pp. 273–284. doi:10.1007/s00158-012-0763-y.

[38] Lyu, Z., and Martins, J. R. R. A., "Aerodynamic Design Optimization Studies of a Blended-Wing-Body Aircraft," *Journal of Aircraft*, Vol. 51, No. 5, 2014, pp. 1604–1617. doi:10.2514/1.C032491.

[39] Secco, N. R., and Martins, J. R. R. A., "RANS-based Aerodynamic Shape Optimization of a Strut-braced Wing with Overset Meshes," *Journal of Aircraft*, Vol. 56, No. 1, 2019, pp. 217–227. doi:10.2514/1.C034934.

[40] Yildirim, A., Gray, J. S., Mader, C. A., and Martins, J. R. R. A., "Performance Analysis of Optimized STARC-ABL Designs Across the Entire Mission Profile," *Proceedings of the AIAA SciTech Forum*, 2021. doi:10.2514/6.2021-0891.

[41] Liao, Y., Yildirim, A., Young, Y. L., and Martins, J. R. R. A., "Hydrodynamic Optimization of a T-foil," *SNAME Maritime Convention*, The Society of Naval Architects and Marine Engineers, 2020. URL https://www.onepetro.org/conference-paper/SNAME-SMC-2020-084.

[42] Dhert, T., Ashuri, T., and Martins, J. R. R. A., "Aerodynamic Shape Optimization of Wind Turbine Blades Using a Reynolds-Averaged Navier–Stokes Model and an Adjoint Method," *Wind Energy*, Vol. 20, No. 5, 2017, pp. 909–926. doi:10.1002/we.2070.

[43] Sederberg, T. W., and Parry, S. R., "Free-form Deformation of Solid Geometric Models," *SIGGRAPH Comput. Graph.*, Vol. 20, No. 4, 1986, pp. 151–160. doi:10.1145/15886.15903.

[44] Kenway, G. K., Kennedy, G. J., and Martins, J. R. R. A., "A CAD-Free Approach to High-Fidelity Aerostructural Optimization," *Proceedings of the 13th AIAA/ISSMO Multidisciplinary Analysis Optimization Conference*, Fort Worth, TX, 2010. doi:10.2514/6.2010-9231.

[45] Luke, E., Collins, E., and Blades, E., "A Fast Mesh Deformation Method Using Explicit Interpolation," *Journal of Computational Physics*, Vol. 231, No. 2, 2012, pp. 586–601. doi:10.1016/j.jcp.2011.09.021.

[46] Kenway, G. K. W., and Martins, J. R. R. A., "Buffet-Onset Constraint Formulation for Aerodynamic Shape Optimization," *AIAA Journal*, Vol. 55, No. 6, 2017, pp. 1930–1947. doi:10.2514/1.J055172.

[47] Mader, C. A., Kenway, G. K. W., Yildirim, A., and Martins, J. R. R. A., "ADflow: An open-source computational fluid dynamics solver for aerodynamic and multidisciplinary optimization," *Journal of Aerospace Information Systems*, Vol. 17, No. 9, 2020, pp. 508–527. doi:10.2514/1.I010796.

[48] Kenway, G. K. W., Mader, C. A., He, P., and Martins, J. R. R. A., "Effective Adjoint Approaches for Computational Fluid Dynamics," *Progress in Aerospace Sciences*, Vol. 110, 2019, p. 100542. doi:10.1016/j.paerosci.2019.05.002.

[49] Yildirim, A., Kenway, G. K. W., Mader, C. A., and Martins, J. R. R. A., "A Jacobian-free approximate Newton–Krylov startup strategy for RANS simulations," *Journal of Computational Physics*, Vol. 397, 2019, p. 108741. doi:10.1016/j.jcp.2019.06.018.

[50] Chauhan, S., and Martins, J. R. R. A., "RANS-Based Aerodynamic Shape Optimization of a Wing Considering Propeller-Wing Interaction," *Journal of Aircraft*, Vol. 58, No. 3, 2021, pp. 497–513. doi:10.2514/1.C035991.

[51] Huang, D., and Friedmann, P. P., "An Integrated Aerothermoelastic Analysis Framework for Predicting the Response of Composite Panels," *15th Dynamics Specialists Conference*, American Institute of Aeronautics and Astronautics, 2016. doi:10.2514/6.2016-1090.

[52] Mader, C. A., and Martins, J. R. R. A., "Derivatives for Time-Spectral Computational Fluid Dynamics Using an Automatic Differentiation Adjoint," *AIAA Journal*, Vol. 50, No. 12, 2012, pp. 2809–2819. doi:10.2514/1.J051658.

[53] Spalart, P., and Allmaras, S., "A One-Equation Turbulence Model for Aerodynamic Flows," *30th Aerospace Sciences Meeting and Exhibit*, 1992. doi:10.2514/6.1992-439.

[54] Lyu, Z., Kenway, G. K., Paige, C., and Martins, J. R. R. A., "Automatic Differentiation Adjoint of the Reynolds-Averaged Navier–Stokes Equations with a Turbulence Model," *21st AIAA Computational Fluid Dynamics Conference*, San Diego, CA, 2013. doi:10.2514/6.2013-2581.

[55] Kennedy, G. J., and Martins, J. R. R. A., "A Parallel Finite-Element Framework for Large-Scale Gradient-Based Design Optimization of High-Performance Structures," *Finite Elements in Analysis and Design*, Vol. 87, 2014, pp. 56–73. doi:10.1016/j.finel.2014.04.011.

[56] Leader, M. K., Chin, T. W., and Kennedy, G. J., "High-Resolution Topology Optimization with Stress and Natural Frequency Constraints," *AIAA Journal*, Vol. 57, No. 8, 2019. doi:10.2514/1.J057777.

[57] Golub, G. H., and Van Loan, C. F., *Matrix Computations*, 4th ed., Johns Hopkins University Press, Baltimore, MD, 2013.

[58] Jonsson, E., Kenway, G. K. W., Kennedy, G. J., and Martins, J. R. R. A., "Development of Flutter Constraints for High-fidelity Aerostructural Optimization," *18th AIAA/ISSMO Multidisciplinary Analysis and Optimization Conference*, Denver, CO, 2017. AIAA 2017-4455.

[59] Jonsson, E., Mader, C. A., Kennedy, G. J., and Martins, J. R. R. A., "Computational Modeling of Flutter Constraint for High-Fidelity Aerostructural Optimization," *2019 AIAA/ASCE/AHS/ASC Structures, Structural Dynamics, and Materials Conference*, American Institute of Aeronautics and Astronautics, San Diego, CA, 2019. doi:10.2514/6.2019-2354.

[60] Kennedy, G. J., "A Full-space Barrier Method for Stress-constrained Discrete Material Design Optimization," *Structural and Multidisciplinary Optimization*, Vol. 54, No. 3, 2016, pp. 619–639. doi:10.1007/s00158-016-1428-z.

[61] Kreisselmeier, G., and Steinhauser, R., "Systematic Control Design by Optimizing a Vector Performance Index," *International Federation of Active Controls Symposium on Computer-Aided Design of Control Systems, Zurich, Switzerland*, 1979. doi:10.1016/S1474-6670(17)65584-8.

[62] Kennedy, G. J., and Hicken, J. E., "Improved constraint-aggregation methods," *Computer Methods in Applied Mechanics and Engineering*, Vol. 289, 2015, pp. 332–354. doi:10.1016/j.cma.2015.02.017.

[63] He, S., Jonsson, E., Mader, C. A., and Martins, J. R. R. A., "Aerodynamic Shape Optimization with Time Spectral Flutter Adjoint," *2019 AIAA/ASCE/AHS/ASC Structures, Structural Dynamics, and Materials Conference*, American Institute of Aeronautics and Astronautics, San Diego, CA, 2019. doi:10.2514/6.2019-0697.

[64] He, S., Jonsson, E., Mader, C. A., and Martins, J. R. R. A., "A Coupled Newton–Krylov Time-Spectral Solver for Wing Flutter and LCO Prediction," *AIAA Aviation Forum*, Dallas, TX, 2019. doi:10.2514/6.2019-3549.

[65] He, S., Jonsson, E., Mader, C. A., and Martins, J. R. R. A., "Coupled Newton–Krylov Time-Spectral Solver for Flutter and Limit Cycle Oscillation Prediction," *AIAA Journal*, Vol. 59, No. 6, 2021, pp. 2214–2232. doi:10.2514/1.J059224.

[66] Wu, N., Kenway, G., Mader, C. A., Jasa, J., and Martins, J. R. R. A., "pyOptSparse: A Python framework for large-scale constrained nonlinear optimization of sparse systems," *Journal of Open Source Software*, Vol. 5, No. 54, 2020, p. 2564. doi:10.21105/joss.02564.

[67] Gill, P. E., Murray, W., and Saunders, M. A., "SNOPT: An SQP Algorithm for Large-Scale Constrained Optimization," *SIAM Review*, Vol. 47, No. 1, 2005, pp. 99–131. doi:10.1137/S0036144504446096.

[68] Bak, C., Zahle, F., Bitsche, R., Kim, T., Yde, A., Henriksen, L. C., Natarajan, A., and Hansen, M., "Description of the DTU 10 MW reference wind turbine," Tech. Rep. DTU Wind Energy Report-I-0092, Danish Technical University, DTU Wind Energy Roskilde, DK, 2013.

[69] Dykes, K., Ning, A., King, R., Graf, P., Scott, G., and Veers, P. S., "Sensitivity Analysis of Wind Plant Performance to Key Turbine Design Parameters: A Systems Engineering Approach," *32nd ASME Wind Energy Symposium*, 2014. doi:10.2514/6.2014-1087, URL https://arc.aiaa.org/doi/abs/10.2514/6.2014-1087.

[70] Ashuri, T., Zaaijer, M. B., Martins, J. R. R. A., van Bussel, G. J. W., and van Kuik, G. A. M., "Multidisciplinary Design Optimization of Offshore Wind Turbines for Minimum Levelized Cost of Energy," *Renewable Energy*, Vol. 68, 2014, pp. 893–905. doi:10.1016/j.renene.2014.02.045.

[71] Ning, A., Damiani, R., and Moriarty, P., "Objectives and Constraints for Wind Turbine Optimization," *Journal of Solar Energy Engineering*, Vol. 136, No. 4, 2014, pp. 041010–1–12. doi:10.1115/1.4027693.

[72] Myhr, A., Bjerkseter, C., Ågotnes, A., and Nygaard, T. A., "Levelised cost of energy for offshore floating wind turbines in a life cycle perspective," *Renewable energy*, Vol. 66, 2014, pp. 714–728.

[73] Kenway, G. K. W., and Martins, J. R. R. A., "Multipoint Aerodynamic Shape Optimization Investigations of the Common Research Model Wing," *Proceedings of the AIAA Science and Technology Forum and Exposition (SciTech)*, Kissimmee, FL, 2015. doi:10.2514/6.2015-0264.

[74] Mangano, M., and Martins, J. R. R. A., "Multipoint Aerodynamic Shape Optimization for Subsonic and Supersonic Regimes," *Journal of Aircraft*, 2021. doi:10.2514/1.C036216.